Supplementary Information for Compact, Low-Loss, High-Speed Graphene Hybrid Modulator

P. Ma[1,2,*], X. Z. Zhang[1], W. Heni[3], N. Floery[4], T. Blatter[1], Y. Horst[1], T. Watanabe[1], C. H. Wang[2], T. Wu[2], B. Li[2], M. R. Sun[2], Z. X. Wang[2], K. Keller[1], M. Burla[1], A. Emboras[5], L. Novotny[4], D. L. Elder[6], L. R. Dalton[6], J. Leuthold[1,3*]

[1]ETH Zurich, Institute of Electromagnetic Fields, 8092 Zurich, Switzerland
[2]University of Science and Technology of China, 230026 Hefei, P. R. China
[3]Polariton Technologies, 8134 Adliswil, Switzerland
[4]ETH Zurich, Photonics Laboratory, 8093 Zurich, Switzerland
[5]ETH Zurich, Integrated Systems Laboratory, 8092 Zurich, Switzerland
[6]University of Washington, Department of Chemistry, WA 98195-1700 Seattle, USA
[*]E-mail: mapi@ethz.ch; leuthold@ethz.ch

Contents

I) Device simulations

Waveguide simulations and geometry optimizations were conducted using a finite-element method (FEM)-based eigenvalue-mode solver (COMSOL Multiphysics). Numerical simulations investigated optical modal characteristics such as single-mode conditions and transmission losses, and evaluated critical performance parameters such as field confinement factors and modulation efficiencies. The graphene was modelled as an anisotropic ultra-thin material with a complex refractive index[1,2]. The in-plane dielectric constant ($\epsilon_{//}$) is derived from the surface conductivity of graphene ($\sigma_{//}$), calculated via the Kubo formalism incorporating inter- and intra-band contributions[3].

$$\sigma_{//}(\omega) = \sigma_{inter}(\omega) + \sigma_{intra}(\omega) \tag{1}$$

$$\sigma_{inter}(\omega) = \frac{\sigma_0}{2}\left(\tanh\frac{\hbar\omega + 2E_F}{4k_BT} + \tanh\frac{\hbar\omega - 2E_F}{4k_BT}\right) - i\frac{\sigma_0}{2\pi}\log\frac{(\hbar\omega + 2E_F)^2}{(\hbar\omega - 2E_F)^2 + (2k_BT)^2} \tag{2}$$

$$\sigma_{intra}(\omega) = i\frac{4\sigma_0}{\pi}\frac{E_F}{\hbar\omega + i\hbar\gamma} \tag{3}$$

with σ_{inter} and σ_{intra} being the inter-band conductivity and intra-band conductivity respectively, $\sigma_0 = q^2/4\eta = 60.85$ μS the universal conductivity of graphene (with $q = 1.6 \times 10^{-19}$C the electron charge), ω the optical angular frequency, $\hbar\omega$ the photon energy, E_F the Fermi level, k_B the Boltzmann constant, $k_BT = 0.026$ eV the thermal energy at room temperature of 300 K, and $\hbar\gamma = 0.0033$ eV the electron relaxation energy (with γ the intra-band scattering rate).

The in-plane and out-of-plane dielectric constants are given by

$$\epsilon_{//}(\omega) = \epsilon_r + \frac{i\sigma(\omega)}{\omega\epsilon_0 h_G} \tag{4}$$

$$\epsilon_{\perp}(\omega) = \epsilon_r \tag{5}$$

with ω being the optical angular frequency, ϵ_0 the dielectric constant of vacuum, ϵ_r the background permittivity and h_G the thickness of graphene.

To calculate the device capacitance, we performed a static 3D simulation using COMSOL Multiphysics. The upper graphene layer was set as a terminal with a bias voltage, while the lower graphene layer was grounded. By sweeping the device lengths, multiple capacitance values proportional to the device lengths were obtained. The capacitance per unit length was extracted as 0.62 fF μm^{-1} for a graphene electrode pair overlapping with a waveguide width.

II) Design of grating couplers and multi-mode interferometers

Grating couplers (GCs) were designed using 3D finite-difference time-domain (FDTD) simulations (Lumerical FDTD software) to efficiently couple laser light from off-chip sources into vertical silicon slot access waveguides on the chip. The design employed structuring of only the top amorphous silicon (a-Si) layer, enabling a simplified fabrication process. The grating period and duty cycle were optimized to maximize fiber-to-chip coupling efficiencies, with an optimal GC achieving >40% efficiency across a 50 nm bandwidth in the C-band (Supplementary Fig. S1a).

In the Mach-Zehnder (MZ) modulator architecture, multimode interference (MMI) couplers serve to split input light into two arms and recombine the output signals. Similarly, as GCs, the MMI structures were fabricated only within the top α-Si layer. The geometries were simulated using Lumerical FDTD software. Critical parameters such as the dimensions of the MMI region and access waveguides, including their lengths and widths were optimized. Input and output access waveguides feature adiabatic tapers to mitigate insertion losses at waveguide interfaces. Simulated top-view modal profile of the MMI coupler (Supplementary Fig.1b) illustrates effective confinement and symmetric power distribution critical to device performance. As the

integrated graphene electrodes minimally perturb the mode profile, the coupling losses between the access waveguides and phase modulators are eliminated.

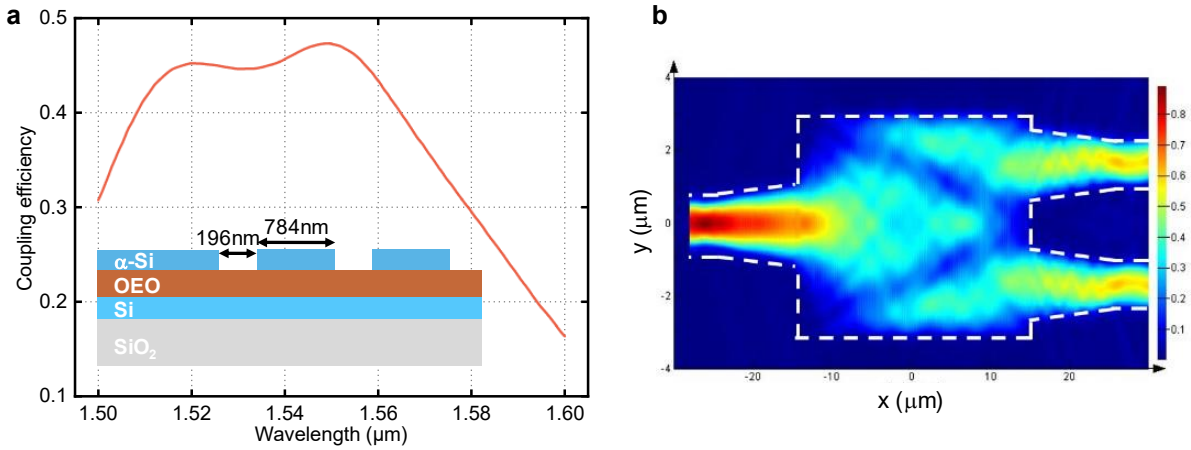

Supplementary Figure S1 | Design and simulations of passive photonic components. a, simulated transmission spectrum of a grating coupler (GC) with an optimized geometry. *Inset:* Layer stack of the GC, highlighting the structured top α-Si layer. **b**, simulated modal field of a multimode interference coupler. Dashed lines outline the contour of the etched α-Si layer.

III) Contact and series resistances of graphene electrodes

The Van der Pauw method was employed to precisely determine the sheet resistances of graphene layers. This four-terminal technique, performed on a symmetrically contacted structure, mitigates contact resistance artifacts, ensuring reliable characterization of the intrinsic electrical properties. Voltage-current measurements were conducted using a Cascade SUMMIT200 probe station and Keysight B1500A Semiconductor Device Parameter Analyzer on several fabricated test structures with multiple contact configurations across the same device chip. The average sheet resistances ($R_{\square}$) of the bottom and top 4-layer graphene were determined to be $285 \pm 19.0\ \Omega/\square$ and $2099.1 \pm 105.5\ \Omega/\square$, respectively.

The contact resistance was determined by measuring the total resistance between two terminals and subsequently isolating the contact contribution by subtracting the sheet resistance from the total resistance. The contact resistivities (ρ_c) of bottom and top graphene layers were extracted to be 229.4 ± 22.9 Ω·μm and 1160.3 ± 62.9 Ω·μm, respectively.

IV) Equivalent circuit model and bandwidth limitation analysis

The device is modeled by an equivalent R-C circuit (Supplementary Fig. S2). Circuital resistances comprise contributions from metal-graphene edge contact resistances ($R_{c1,2}$) and graphene series resistance ($R_{s1,2}$) of graphene electrodes in both non-gated ($R_{g1,2}$) and gated regions ($R_{ng1,2}$). The subscripts 1 and 2 denote the bottom and top graphene electrodes, respectively. The non-gated region width (W_{ng}) was minimized to reduce the series resistance of graphene while avoiding parasitic losses associated with metal contact pads (Supplementary Fig. S3). The capacitance (C) arises from graphene's quantum capacitance (C_Q) and a series-connected parallel-plate capacitor structure, where the organic electro-optic (OEO) thin film acts as the primary dielectric interlayer.

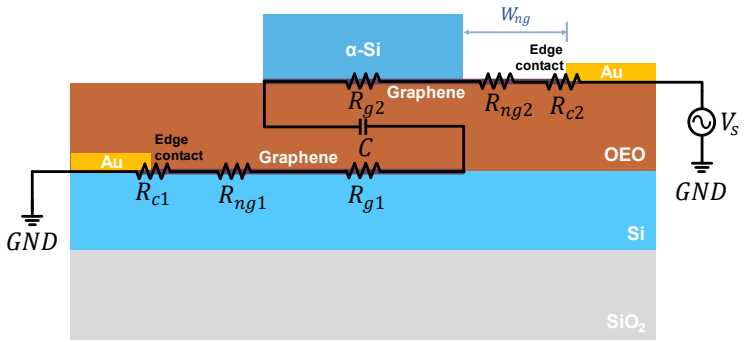

Supplementary Figure S2 | Equivalent circuit of graphene-organic-silicon hybrid modulator. $R_{c1,2}$, $R_{ng1,2}$ and $R_{g1,2}$ represent the contact, non-gated and gated series resistances of the bottom and top graphene electrode layer, respectively. C denotes the capacitance of the device.

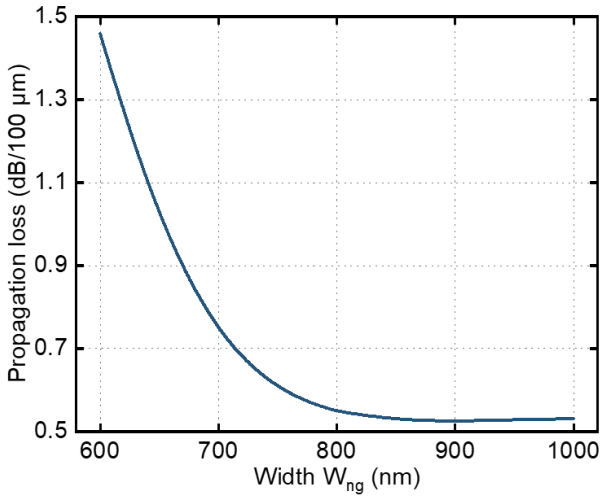

Supplementary Figure S3 | Simulated propagation losses of the phase modulator with varying the widths of the non-gated region of graphene electrodes (W_{ng}).

With sheet resistances ($R_{\square}$) and contact resistivities (ρ_c), the series and contact resistances can be derived as

$$R_c = \frac{\rho_c}{L_c} \tag{6}$$

$$R_{ng} = \frac{R_{\square} W_{ng}}{L_{ng}} \tag{7}$$

$$R_g = \frac{R'_{\square} W_g}{2L_g} \tag{8}$$

where L_c is the length of the contact length. W_{ng} and L_{ng} are the width and length of the non-gated graphene region, respectively. W_g and L_g are the width and length of the gated graphene region, respectively. As our device design minimizes the charge-loading effect in graphene, for simplicity, the sheet resistance was modeled as uniform across the entire graphene region. After substituting the measured sheet resistances and contact resistivities, the total contact resistance $R_c = R_{c1} + R_{c2} = 55.6 \pm 3.4\ \Omega$ and the total series resistance $R_s = R_{ng1} + R_{ng2} + R_{g1} + R_{g2} = 137.3 \pm 7.3\ \Omega$. The total resistance is $R = R_c + R_s + R_d = 242.9 \pm 10.7\ \Omega$, where R_d is the driver impedance of 50 Ω.

The quantum capaticance contains conbribution from both bottom and top graphene layers[1].

$$C_{Q1,2} = \frac{2W_g L q k_B T}{\pi(\hbar v_F)^2} \log\left[2\left(1 + \cosh\frac{E_F}{k_B T}\right)\right] \tag{9}$$

with W_g being the width of the overlap region between top and bottom graphene, L the length of the modulator, $q = 1.6 \times 10^{-19}$ coulombs the electron charge, k_B the Boltzmann constant, $k_B T = 0.026$ eV the thermal energy at room temperature of 300 K, $\hbar$ the reduced Planck's constant, $v_F = 9.5 \times 10^7 \text{cm sec}^{-1}$ the Fermi velocity in graphene, $E_F = 300$ meV the Fermi level. The total quantum capacitance was calculated to be 4.28 pF, while the parallel-plate capacitance was simulated to be 15.75 fF for a 25 μm long device. As the quantum capacitance exceeds the parallel-plate capacitance by two orders of magnitude and these capacitances are connected in series, the total capacitance is predominantly governed by the parallel-plate capacitance.

The 3-dB cut-off bandwidth (f_{est}) can be estimated by

$$f_{est} \approx \frac{1}{2\pi RC} \tag{10}$$

The calculated bandwidth of 42.2 GHz aligns closely with the measured value of 40.2 GHz. Theoretical analysis confirms the device bandwidth is currently RC-limited, dominated by graphene electrodes' contact and sheet resistances. However, this limitation stems from current fabrication constraints and is addressable through technological development. Graphene's intrinsic semi-metallic nature enables ultra-low resistance values, as demonstrated in prior studies reporting sheet resistances of 40 Ω per square[4] and edge-contact resistances of 2.57 Ω·μm [5]. With these numbers of graphene electrodes, for the present design, series and contact resistances are calculated to be 5.76 Ω and 0.2 Ω, respectively. The potential RC-limited 3-dB bandwidth is roughly 183 GHz with a 50 Ω driver, exceeding 1.8 THz when considering only the device impedance.

V) Graphene's carried-induced phase modulation

Application of an external voltage charges the parallel-plate capacitor through graphene electrodes, altering the carrier density and shifting the Fermi level of graphene. This modifies graphene's surface conductivity and dielectric constant, as described by Equations (1)-(4). In practice, charges redistribute rapidly in graphene due to diffusive carrier dynamics. For computational simplicity, we assume that capacitive loading induces carrier density changes and Fermi level shifts only within the gated-graphene region. The carrier density change (ΔN) is calculated as

$$\Delta N = \frac{\Delta Q}{A} = \frac{C_u \cdot \Delta V}{A} \tag{11}$$

where ΔQ is the charge change per unit device length; C_u is the unit capacitance; ΔV is the applied voltage change, and A is the area of the gated graphene region.

Simulated carrier density changes in graphene under 0 V and 5 V bias voltages at different initial Fermi levels are shown in Supplementary Fig. S4a. Applied biases induce almost consistent carrier density changes across various initial Fermi levels, with minor variation. Supplementary Figure S4b reveals that the carrier density shifts induce varying Fermi level displacements depending on the initial Fermi levels: heavily doped graphene with a high Fermi level exhibits small Fermi level shifts, while lightly doped graphene with an initial Fermi level near the Dirac point achieves large shift up to 0.16 eV.

We simulated the effective refractive index modulation across a Fermi level range of 0-0.8 eV (Supplementary Fig. S5). The simulation results reveal that graphene-induced modal effective index changes are negligible compared to those driven by the Pockels effect in organic polymers. Specifically, graphene's carrier-induced phase modulation corresponds to an effective voltage-length product $U_\pi L > 2.5 \times 10^4$ V · μm, much larger than 500 V · μm achieved via the organic electro-optic Pockels effect. This confirms that phase modulation in

the hybrid system is dominated by the Pockels effect in the organic polymer, rather than carrier density shifts in graphene. Consistent with this, we did not observe phase modulation in devices prior to the activation of organic functional materials.

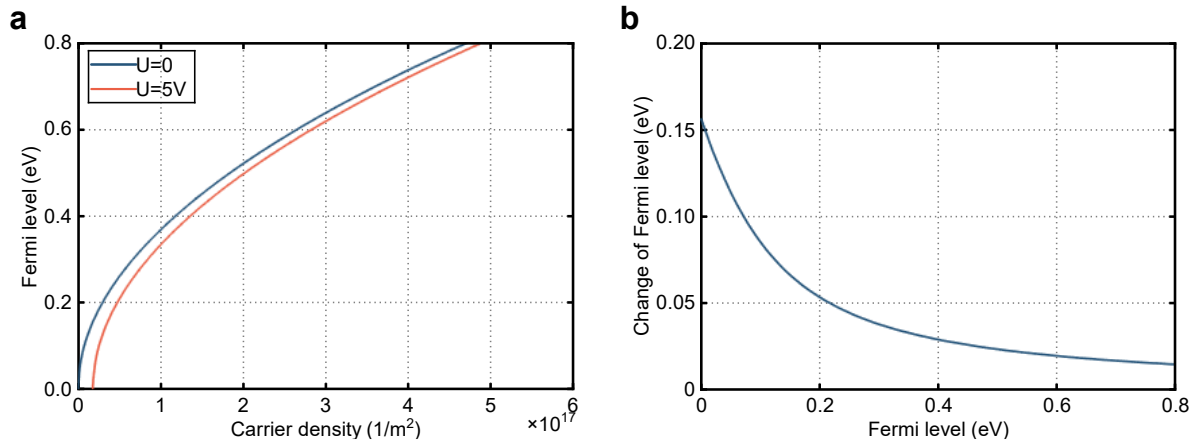

Supplementary Figure S4 | Impact of capacitive charging on graphene's Fermi levels. a, carrier density changes in graphene under a 5 V applied bias. Red and bule curves represent initial and post-bias carrier densities, respectively, for different initial Fermi levels. **b,** Fermi level shifts induced by capacitive loading for different initial Fermi levels. Lower initial Fermi levels (e.g., near the Dirac point) exhibit larger shifts up to 0.16 eV, while heavily doped regimes (high initial Fermi levels, e.g., >0.3 eV) show small changes.

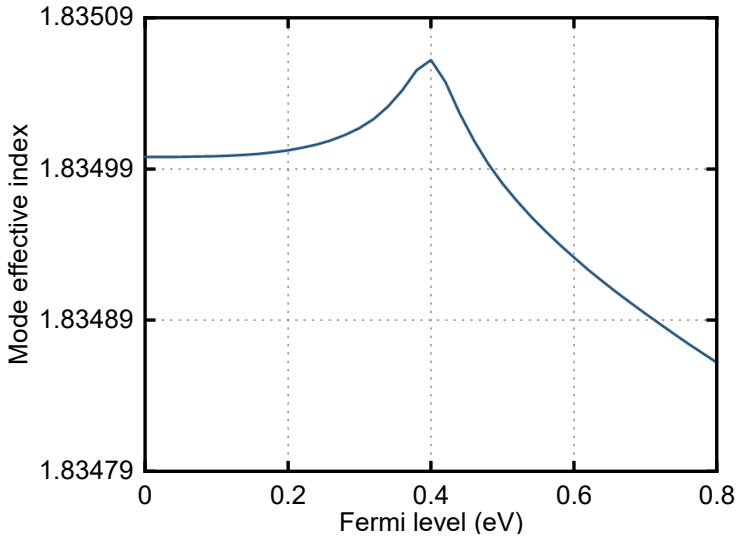

Supplementary Figure S5 | Simulated modal effective index to graphene's Fermi level variations. Simulations reveal minimal modulation of the modal effective index even with large Fermi level shifts spanning 0 to 0.8 eV. The observed small index change (<0.0003) highlights weak electro-optic tunability in graphene of the present device.

Reference

1. Agarwal, H. *et al.* 2D-3D integration of hexagonal boron nitride and a high-κ dielectric for ultrafast graphene-based electro-absorption modulators. *Nat. Commun.* **12**, 1070 (2021).
2. Meng, Y. *et al.* Waveguide Engineering of Graphene Optoelectronics—Modulators and Polarizers. *IEEE Photonics J.* **10**, 1–17 (2018).
3. Hanson, G. W. Dyadic Green's functions and guided surface waves for a surface conductivity model of graphene. *J. Appl. Phys.* **103**, 064302 (2008).
4. Wang, L. *et al.* One-Dimensional Electrical Contact to a Two-Dimensional Material. *Science* **342**, 614–617 (2013).
5. Keramatnejad, K. *et al.* Laser-Assisted Nanowelding of Graphene to Metals: An Optical Approach toward Ultralow Contact Resistance. *Adv. Mater. Interfaces* **4**, 1700294 (2017).